The Effect of Hawai'i's Big Island on Track and Structure of Tropical Cyclones Passing to the South and West*

CHRISTOPHER R. S. CHAMBERS

Department of Meteorology, University of Hawaii at Manoa, Honolulu, Hawaii

TIM LI

International Pacific Research Center, and Department of Meteorology, University of Hawaii at Manoa, Honolulu, Hawaii

(Manuscript received 1 February 2011, in final form 9 May 2011)

ABSTRACT

The effect of the Big Island of Hawai'i on tropical cyclone (TC) track and structure is investigated using the Weather Research and Forecasting (WRF) model. The high (~4000 m) mountains of the Big Island modulate lower-tropospheric flow in such a way that it can influence TCs hundreds of kilometers away from the island. When a TC approaches from the east, the blocking of lower-tropospheric flow leads to a slowing of the TC's movement. As a TC passes close to the south side of the Big Island, it deviates southward. The TC core convection and winds can become axisymmetric because of the blocking of the stronger northeasterly flow to the north of the storm. The authors hypothesize that this axisymmetrization led to the unexpected eye formation of Hurricane Flossie (2007) just southeast of the Big Island. As a TC moves into the lee (southwest side) of the Big Island, the flow associated with the island wake leads to a track deviated to the right. The Hurricane Dot (1959) simulations suggest that this effect contributed to an observed deviation to the north, which led to eventual Kauai landfall. A greater TC intensity is found in the lee of the Big Island compared to the case without the island, which is primarily attributed to a weakened vertical wind shear associated with the island blocking.

1. Introduction

The Big Island of Hawai'i (BI) is the smallest island in the world (surface area = 10 432 km^2) that has mountains over 4000 m high. This unique topography has profound implications for the flow regime over and around the island. Smith (1989) noted that high mountains with small aspect ratios stagnate the airstream on the windward slope before wave breaking occurs aloft, which leads to upwind flow splitting. Smorlarkiewicz and Rotunno (1989) showed that for an obstacle similar to the BI the transition from Fr = 0.66 to Fr = 0.22 (Fr = U/Nh where U is the wind speed, N is the buoyancy frequency, and h is the height of the mountain obstacle) produced a change in the flow regime from flow over, to flow around the obstacle. Taking typical trade wind conditions of $N = 0.01\ \mathrm{s}^{-1}$, $U = 10\ \mathrm{m\ s}^{-1}$, and a mountain height of 4100 m, we get Fr = 0.24. This implies that under trade wind conditions the BI is rooted in a blocked flow regime. Chen and Feng (2001) found that diabatic heating enhances vertical motions in cloudy areas over the windward side of the BI and consequently weakens island blocking.

In this study we investigate the changes in tropical cyclone (TC) track and structure that are attributable to the presence of the BI. Previous studies of the impacts of island topography on TCs have mostly focused on Taiwan. Chang (1982) found that a modeled TC approaching Taiwan underwent a weakening as the mountain blocked the low-level circulation. Tropical cyclone movement near the island was governed largely by the disturbed low-level flow rather than by the midtropospheric winds. A numerical modeling study by Bender et al. (1985) found that as a TC approached a coastal mountain range from the east, convergence of moisture occurred east of the mountains, which helped to maintain the TC's intensity before

* School of Ocean and Earth Science and Technology Contribution Number 8203 and International Pacific Research Center Contribution Number 792.

Corresponding author address: Christopher Chambers, Department of Meteorology, University of Hawaii at Manoa, 2525 Correa Rd., Honolulu, HI 96822.
E-mail: crc@hawaii.edu

DOI: 10.1175/MWR-D-11-00031.1

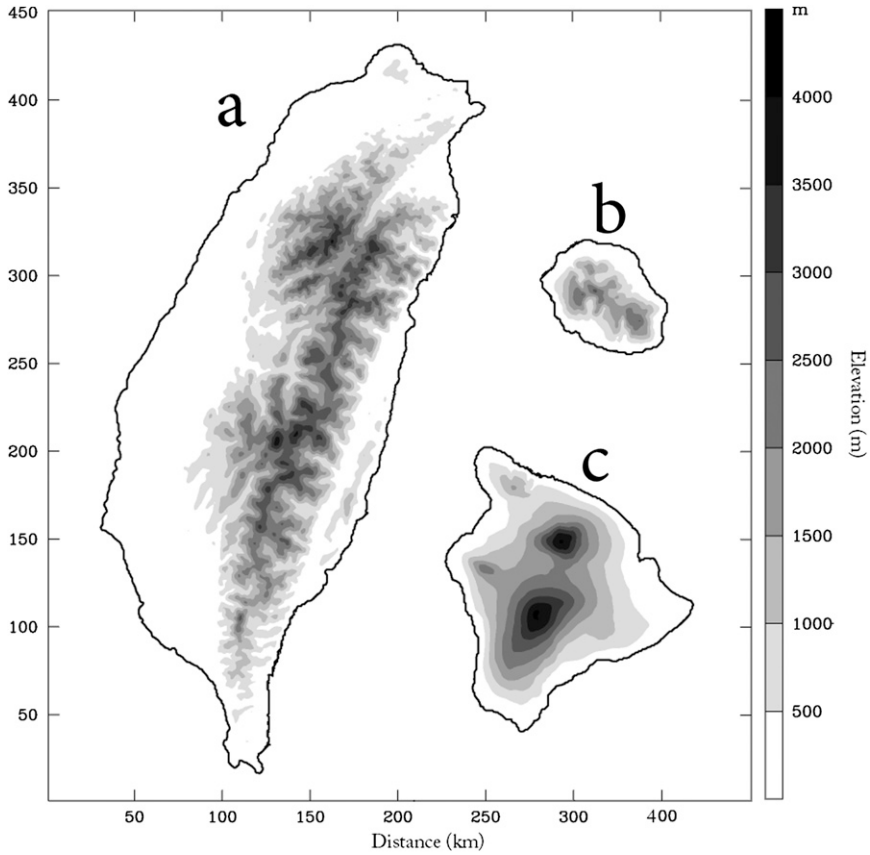

FIG. 1. A comparison of size and topography of (a) Taiwan, (b) Reunion, and (c) the Big Island of Hawai'i.

landfall. Yeh and Elsberry (1993) suggested that the blocking and deflection of the environmental flow by the topography causes zonal decelerations and southward track deflections of TCs. Upstream deflection of TCs approaching Taiwan was larger for weaker and slower-moving storms. A simulation of Supertyphoon Haitang (Jian and Wu 2008) showed that northerly advective flow, caused by the funneling of low-level flow between the mountains and the storm core, led to a southward deflection in track as the TC approached Taiwan. In an observational study of Reunion Island, Roux et al. (2004) suggested that a deviation in track of TC Dina (2002) was caused by island blocking of the low-level flow. Lin et al. (2005) found that the basic flow Froude number dominates the track deflection, with the lower Froude number producing larger track deflection, while the vortex Froude number dominates the track discontinuity for idealized TC vortex passing over the idealized elongated mountain range. Greater track deflections also occurred when the basic flow Rossby number was larger and if the topography was steeper.

A comparison of island size and topography in Fig. 1 shows that the BI has an area approximately 4 times larger than Reunion but less than a third of Taiwan. The two main mountain peaks on the BI [Mauna Kea (4205 m) and Mauna Loa (4169 m)], are both higher than the highest points in Taiwan (3952 m) and Reunion (3070 m).

As a TC approaches the BI the wind speed increase over the island will increase the Froude number. In addition, given the dominant stable trade wind environment present over the Hawaiian Islands, the approach of a TC core will also herald the approach of more unstable conditions. This should tend to decrease the average buoyancy frequency N and thereby further increase the Froude number. Once the convective area associated with a TC is over the BI one would expect greater diabatic heating and a removal of the trade wind inversion. Thus, stronger winds, weakened stability, and greater diabatic heating mean that the transition from normal trade wind conditions to TC conditions should be associated with weakened island blocking and greater flow over the mountain.

Central and eastern Pacific TCs tend to have smaller wind radii (for specified wind speeds) than storms in other basins (Knaff et al. 2007). Factors such as initial vortex size (Xu and Wang 2010) and environmental humidity (Hill and Lackmann 2009) are important in determining

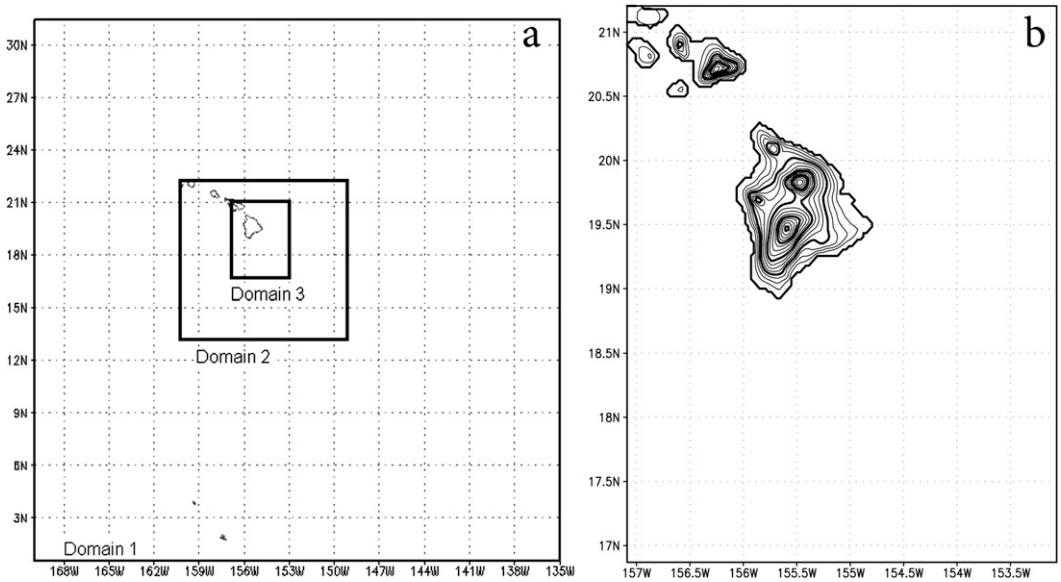

FIG. 2. (a) Outlines of the model domains: domain 1 (whole map, 27-km resolution), domain 2 (9-km resolution), and domain 3 (3-km resolution) and (b) terrain height (m, thick contours plotted every 1000 m, thin contours plotted every 250 m) at domain 3 (3-km resolution).

TC size. The low humidity in the midlevels of the central Pacific atmosphere may be a key factor in explaining the prevalence of small TCs but both factors are relevant. Out of the six nondimensional parameters defined in Lin et al. (2005) as being important for TC track deflection due to island orography, two are dependent on the size of the radius of maximum winds. Therefore the scale of the storm's inner-core winds is an important factor in TC track deflection and/or continuity across the topography.

The objective of this study is to investigate, through a number of numerical model experiments, the effect of the BI topography on central Pacific TCs that approach the Hawaiian Islands from the southeast. Through the idealized and real-case TC simulations, we intend to examine what influence the BI topography has in determining TC characteristics as they pass nearby and what is the sensitivity of the BI impact to initial vortex latitudinal displacement. In section 2 we briefly describe the model experiments and TC cases selected. In sections 3 and 4 we show the simulation results and discuss physical processes responsible for the TC track and structure changes. In section 5 we summarize the major results. A more extensive description of this research is available in Chambers (2008).

2. Model experiment design and case selection

a. Model setup

The Advanced Research Weather Research and Forecasting (ARW-WRF) model version 2.2 (Skamarock et al. 2005) is used for this study. The Perdue–Lin microphysics scheme (Lin et al. 1983), the Betts–Miller–Janjic cumulus scheme (Betts and Miller 1986), and the Yonsei University boundary layer scheme (Noh et al. 2003) are used. The land surface model contains 5 thermal diffusion layers and the atmosphere has 27 terrain-following sigma levels. For the cases before 1999 (Dot and Iniki), initial and lateral boundary conditions are derived from the 2.5° National Centers for Environmental Prediction–National Center for Atmospheric Research (NCEP–NCAR) reanalysis data. For the Flossie simulations the 1° NCEP final analysis and the NCEP real-time sea surface temperature analyses are used. The 30-s resolution U.S. Geological Survey (USGS) terrestrial data are used for the terrain initialization. The model contains three domains at resolutions of 27, 9, and 3 km, respectively (Fig. 2a). The dimensions of the three model domains are given in Table 1. Figure 2b illustrates the model domain 3 topography. The maximum mountain height at this resolution (3 km) is 4040 m and occurs at the Mauna Loa summit, which is 129 m lower than the actual height of 4169 m.

The initial data contain only a weak vortex so a bogus TC is specified in the initial condition. Table 2 lists the

TABLE 1. Dimensions of three model domains.

Domain No.	Resolution (km)	No. of grid points in x direction	No. of grid points in y direction
1	27	146	136
2	9	142	124
3	3	151	172

TABLE 2. Initial bogus vortex parameters for each of the TC cases where RMW is the radius of maximum wind, Vmax is the maximum wind speed, Tx and Ty are the grid point locations of the initial TC center at domain 1, and r is the radius of the vortex.

TC case	RMW (km)	Vmax (m s^{-1})	Tx	Ty	r (km)
Dot	150	45	79	69	270
Iniki	150	45	83	53	
Flossie	150	45	89	62	

initial bogus parameters for each of the TC cases. The TC initialization uses a nonlinear balance equation in sigma coordinates following Wang (1995). The vertical structure of an example vortex is described in Wang (1995, their Figs. 4 and 5). The vertical tangential wind structure is axisymmetric and given as a sine function of the vertical coordinate (σ) corresponding to a midtropospheric warm core. The undisturbed temperature profile is obtained from the western North Pacific sounding of Gray (1975). Tests were performed to determine the bogus setup that best matches observed intensities and structure after 12–24 h of simulation spinup.

To examine the BI effect, two parallel experiments are conducted for each case. In the control experiment the BI topography is retained while in the sensitivity experiment the BI is removed by changing the BI land grids to open-ocean grids. The initial atmospheric and surface conditions at the original BI grids are obtained by interpolating the surrounding ocean environmental conditions. After the simulation starts this section of the atmosphere is quickly mixed, leaving no evidence of the island removal process.

b. Selected TC cases

In this study we will focus on simulating three representative central Pacific TCs. They are Hurricane Dot in 1959, Hurricane Iniki in 1992, and Hurricane Flossie in 2007. For each case, various idealized experiments with the TC location slightly shifted northward or southward are conducted to examine the sensitivity of the BI impact

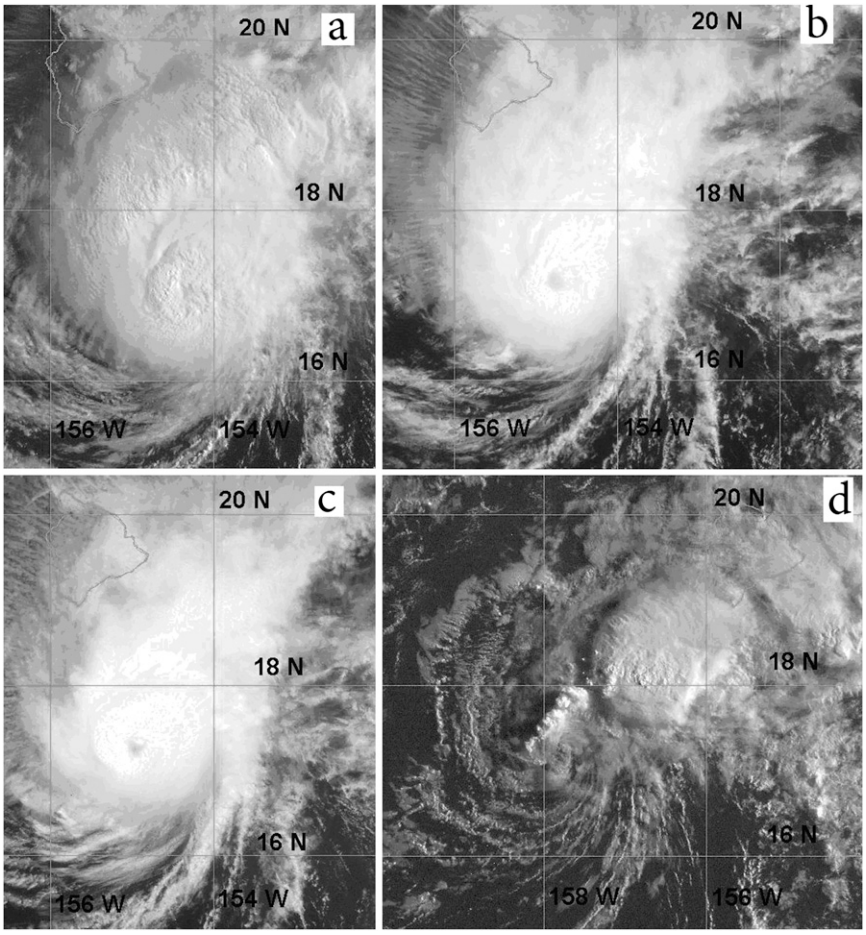

FIG. 3. Visible satellite imagery of Flossie for (a) 1730 UTC 14 Aug, (b) 2030 UTC 14 Aug, (c) 2200 UTC 14 Aug, and (d) 1700 UTC 15 Aug.

TABLE 3. Details of all case simulations.

Tropical cyclone name and year	Simulation name	Big Island (Y/N)	Start date and time	End date and time	Bogus vortex displacement from control
Dot (1959)	DotBI_0	Y	1200 UTC 4 Aug 1959	1200 UTC 7 Aug 1959	0
	DotnoBI_0	N			
	DotBI_S4	Y			4 south (−108 km)
	DotnoBI_S4	N			
	DotBI_N2	Y			2 north (+54 km)
	DotnoBI_N2	N			
	DotBI_N4	Y			4 north (+108 km)
	DotnoBI_N4	N			
Iniki (1992)	IBI_0	Y	0000 UTC 9 Sep 1992	0000 UTC 13 Sep 1992	0
	InoBI_0	N			
	IBI_N3	Y			3 north (81 km)
	InoBI_N3	N			
Flossie (2007)	FBI_0	Y	1200 UTC 13 Aug 2008	1200 UTC 17 Aug 2008	0
	FnoBI_0	N			
	FBI_N3	Y			3 north (81 km)
	FnoBI_N3	N			
	FBI_N6	Y			6 north (162 km)
	FnoBI_N6	N			
	FBI_N9	Y			9 north (243 km)
	FnoBI_N9	N			
	FBI_N12	Y			12 north (324 km)
	FnoBI_N12	N			

to initial TC location, and to obtain robust topographic impact features.

Hurricane Dot (1959) tracked south of the BI before deviating north and making landfall on Kauai. This case is used to investigate whether the influence of BI topography played a role in the marked change in track that occurred after passing south of the BI. This case study is also used for a series of sensitivity studies in which the storm is shifted progressively northward to determine the effects of tracks closer to the BI.

Hurricane Iniki (1992) was the most destructive hurricane to hit the state of Hawai'i in recorded history causing extensive damage to the island of Kauai. The case provides an example of an intense hurricane moving toward the islands from the south. This northward movement was due to of the development of a southerly steering flow associated with an upper-level trough and a surface low pressure to the northwest. Iniki peaked in intensity with 64 m s^{-1} sustained winds and a minimum surface pressure of 938 hPa, at 2100 UTC 11 September, when it was only 210 km south southwest of Lihue, Kauai. Hurricane Iniki made landfall on Kauai at 0130 UTC as the most intense TC on record ever to strike the Hawaiian Islands with maximum sustained winds of 63 m s^{-1}. The storm's impact was enormous and left a long-lasting legacy of environmental and economic damage.

The Iniki case provides an example of a TC approaching from the south that under east or southeasterly large-scale flow allows the storm to interact with the wake of the BI. In addition, by shifting the initial bogus position it will be shown that an Oahu landfall can be simulated. For accurate forecasts to be made it is essential to gain a perspective of the factors that influence the behavior of a TC in this catastrophic scenario.

Hurricane Flossie (2007) maintained category 4 strength until 13 August when it was centered near 15.1°N, 150.1°W. Stronger vertical shear associated with an upper-level trough that had developed north of the islands, combined with marginal SSTs, lead to a weakening of Flossie late on 13 August when its eye became obscured by cloud cover. However a National Weather Service (NWS) forecast discussion on 14 August stated that Flossie's eye "briefly cleared in visible and warmed in infrared imagery earlier today." This occurred "despite the estimate of 30 mph (13.4 m s^{-1}) of southwesterly environmental vertical wind shear in the vicinity of the hurricane at that time." This unexpected period of reorganization is shown on Figs. 3a–c. Following this, through 14 August, Flossie began to move to the left of the forecasted track and underwent spectacular weakening during the night of 14–15 August. By 0200 HST 15 August Flossie weakened to a tropical storm, and to a tropical depression by 2000. On that day the low-level circulation lay outside of the TC's central dense overcast (Fig. 3d), which is universally recognized as a symptom of shear and is often associated with weakening (Dvorak 1984). By the early morning hours of 16 August, the tropical depression was devoid of deep convection and all that was left was a low-level cloud

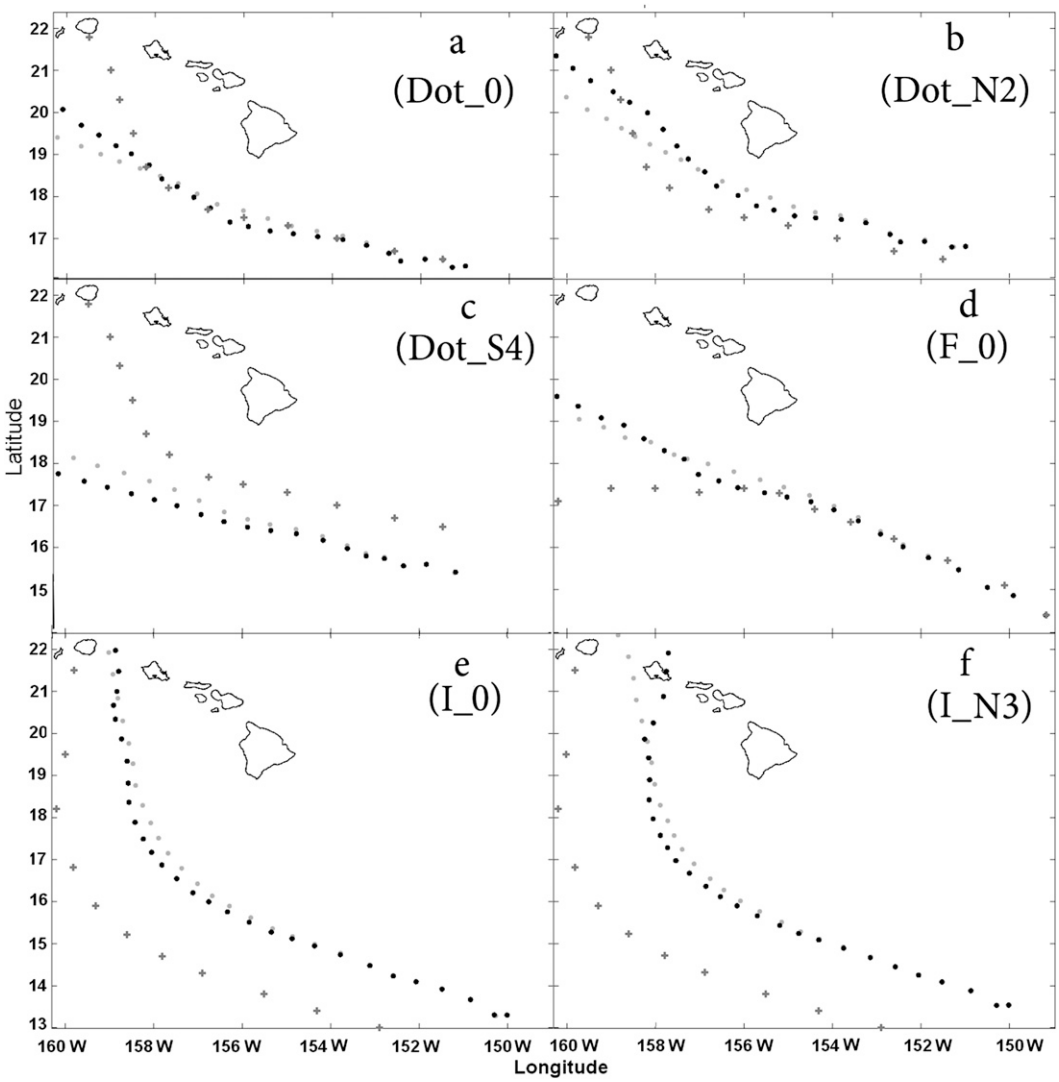

FIG. 4. (a) Dot_0, (b) Dot_N2, (c) Dot_S4, (d) F_0, (e) I_0, and (f) I_N3 simulated tracks (determined by the location of minimum surface pressure) plotted on domain 2 with dots every 3 h. The black (light gray) dots represent the case with (without) the Big Island. The medium gray crosses show the best-track position every 6 h.

swirl. Flossie's closest approach was 185 km south of South Point with sustained winds of 39 mph (17.4 m s^{-1}) reported at South Point.

3. Simulation results and comparison with observations

For brevity a number of acronyms are used to refer to the individual cases. Details of the individual simulations are in Table 3. The "0" in DotBI_0 states that this is the simulation with the most realistic track over the first 48 h. DotnoBI_0 is the same case, but with the BI removed. For simulation DotBI_N2, the "N2" indicates that the initial TC is positioned 2 coarse-resolution grid points (54 km) north of DotBI_0. In the following subsections, a brief overview of each simulated TC track is presented.

a. Dot (1959)

Three cases (DotBI_0, DotBI_N2, and DotBI_S4) aim to replicate the observed storm behavior. DotBI_0 tracks closest to reality and is considered the control case. DotBI_0 follows the observed track best up to 158°W (Fig. 4a) where the real storm's sharp northward shift in track is not replicated accurately. Consequently DotBI_0 fails to simulate the Kauai landfall. Relative to DotnoBI_0, DotBI_0 begins a deviation to the south near 153°W before deviating north near 156°W. There is also a slight slowing of translational speed for DotBI_0 between 154° and 156.5°W.

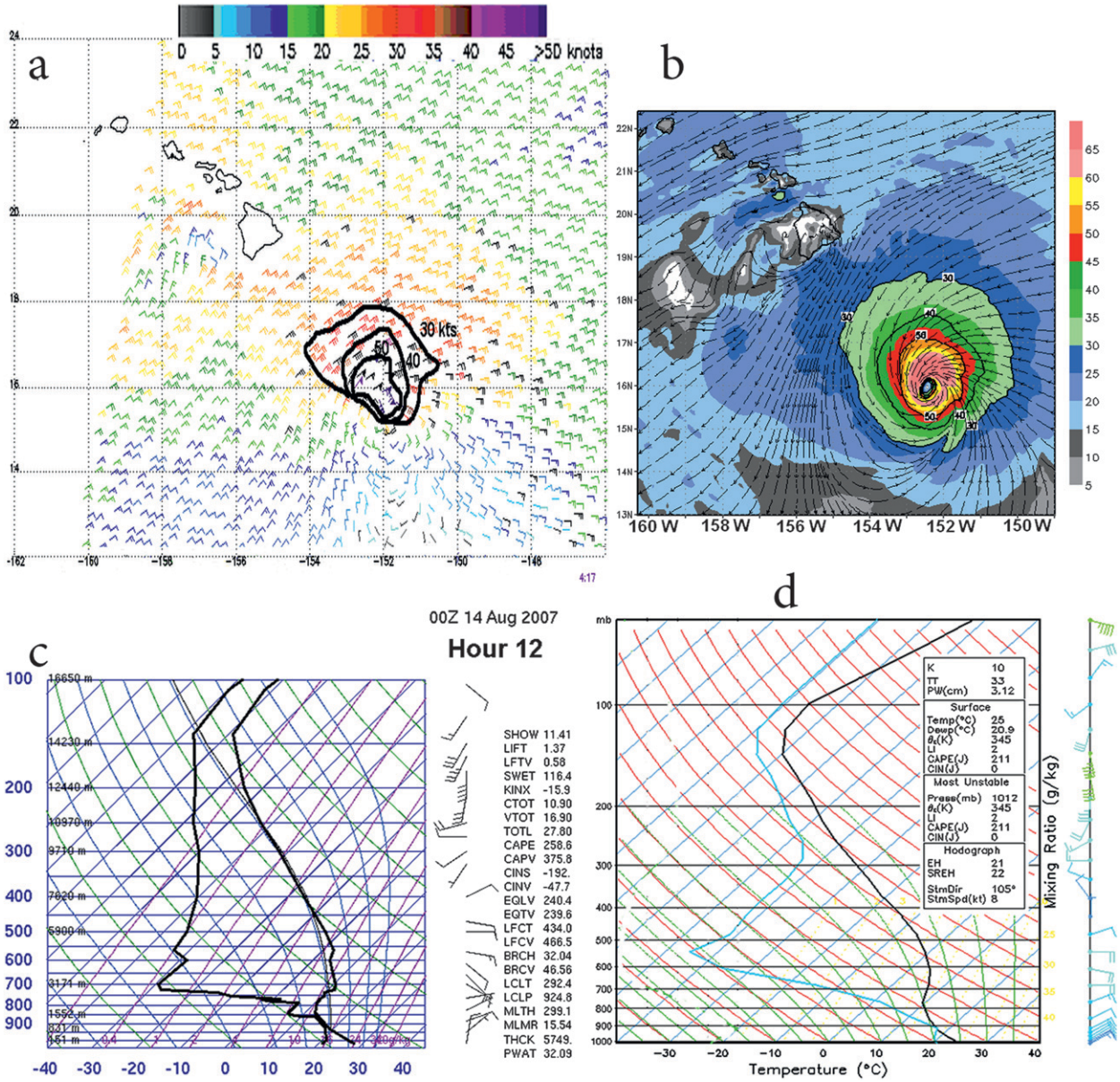

FIG. 5. A comparison of (a) QuikSCAT 10-m surface wind barbs and (b) model 10-m wind speeds (colors) and streamlines for the control Flossie simulation (FBI_0) at hour 21 on domain 2. Black contours outline the 30-, 40-, and 50-kt isotachs (1 kt = 0.5144 m s^{-1}). Both plots are the same scale. (bottom) A comparison of (c) the Hilo sounding of 0000 UTC 14 Aug 2007 and (d) the model sounding at the same location and time. At this time Flossie was located 750 km to the southeast of the BI.

Figure 4b shows a similar though lesser southward deviation for DotBI_N2. Between 155° and 158°W DotBI_N2 exhibits a gradual shift to a more northerly component that continues to 158°W. This track change exhibits a pattern similar to the best track but it is shifted north and east. This does not occur for DotnoBI_N2 indicating that the BI is responsible for the track change. West of 158°W DotBI_N2 turns more westward and begins to parallel DotnoBI_N2 about 85 km farther north. This leads to a similar failure as seen in DotBI_0 to move the storm as far north as observed.

DotBI_S4 has the storm initialized four grid points south (108 km) of DotBI_0. Figure 4c shows that DotBI_S4 also deviates to the south, beginning near 153°W; however, there is no longer the northward shift in track near 156.5°W as seen in DotBI_0 and DotBI_N2. Comparable track changes in the Dot cases with the BI can be seen in the Flossie cases; for example, FBI_0 (Fig. 4d)

shows a southward then northward deviation similar to DotBI_0 and DotBI_N2.

b. Iniki (1992)

Simulations IBI_0 and InoBI_0 track between Kauai and Oahu as shown in Fig. 4e. The end location of simulation IBI_0 is very similar to InoBI_0; however, IBI_0 tracks more westward as it passes 325 km southwest of the BI. Once IBI_0 has reached the latitude of Kauai it actually lies slightly to the east of InoBI_0 because IBI_0 takes a sharper turn to the north.

By shifting the initial vortex farther north, the IBI_N3 case leads to an Oahu landfall (Fig. 4f). At its closest approach IBI_N3 passes about 300 km to the southwest of the BI. This closer approach when compared to IBI_0 appears to be responsible for a more marked rightward turning of IBI_N3. IBI_N3 deviates first to the west of InoBI_N3 and then near 20°N it passes to the east. By the time the IBI_N3 is north of Oahu it lies 115 km to the east of InoBI_N3.

c. Flossie (2007)

During the first 12 h, simulation FBI_0 shows slightly better agreement with the best track than FnoBI_0 (Fig. 4d). West of 156°W both simulations move the storm northwest when the storm actually moved west. A comparison with the Quick Scatterometer (QuikSCAT) winds shown in Fig. 5 reveals that the modeled storms have a reasonable size but a larger area of strongest winds. Asymmetries in the model wind field are evident with stronger winds on the northern side, consistent with QuikSCAT, however the model produces stronger westerly flow in the southern eyewall of a larger eye. Both the model and the QuikSCAT pass show a relatively calm wake spreading southwestward from the BI.

Soundings taken at Hilo on the east coast of the BI are compared to model soundings taken from FBI_0 when Flossie was located roughly 750 km to the southeast (Fig. 5). Both the model and the observations agree that the BI was under trade wind conditions with an observed convective available potential energy of 258 J kg^{-1}, which compares well with the model's 211 J kg^{-1}. The simulation's 27 levels produce a smoother trade wind inversion than the observations.

FBI_0 undergoes more rapid rises in central pressure than FnoBI_0 over the first 48 h of the simulations as shown in Fig. 6. Toward the end of the simulation, the two simulations end up with similar minimum pressures. The pressure traces agree fairly well with the observations that also show progressive weakening. The weakening of Flossie was driven largely by the storm's progression into a region of large-scale vertical wind shear associated with an upper-level trough.

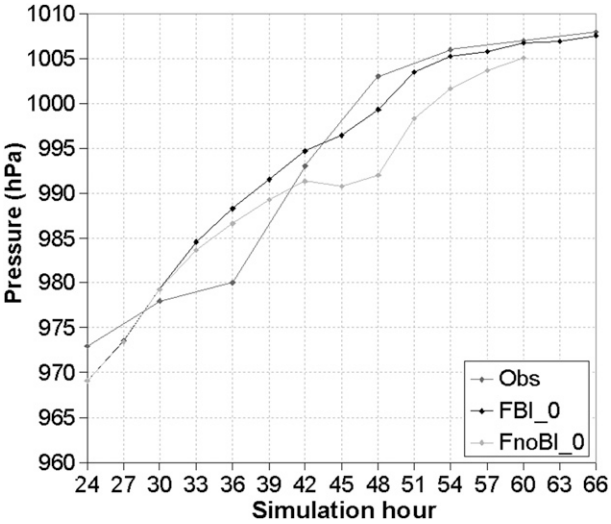

FIG. 6. Observed and simulated minimum sea level pressure evolutions from the FBI_0 and FnoBI_0 cases.

Shifting the initial vortex 3 grids northward leads to an initialization closer to the observed location of the actual storm. Figure 7a shows that FBI_N3 and FnoBI_N3 move north of the observed track. FBI_N3 agrees better with the observations than FnoBI_N3 up to 156°W where a sharp slowing and deviation to the north occurs in the simulation.

Shifting the initial vortex 3 grid points farther north in simulation FBI_N6 and FnoBI_N6 produces a different track (Fig. 7b) with FBI_N6 remaining south of FnoBI_N6 after a gradual deviation to the south starting at 152°W. FBI_N6 produces the most marked slowing of movement south of the BI of any of the simulations, coming to a near standstill near 155°W.

Interestingly, initializing the storm 9 and 12 grid points to the north (Figs. 7c,d) leads to the closest track to the observed storm to the west of BI. This may be because these cases weaken more rapidly than the cases farther to the south because of cooler waters and stronger shear to the north. This leads to a shallower storm whose steering should be governed more by the lower-tropospheric northeasterly flow that acts to steer it southwestward.

4. Characteristic TC track and structure changes associated with the BI impact

a. Slowing of TC when approaching the BI

Several simulations show a slowing of the translational speed of the storm center as it approaches the BI from the east or southeast. This is apparent in the simulations of Flossie (FBI_0, FBI_N3, FBI_N6, FBI_N9, and FBI_N12),

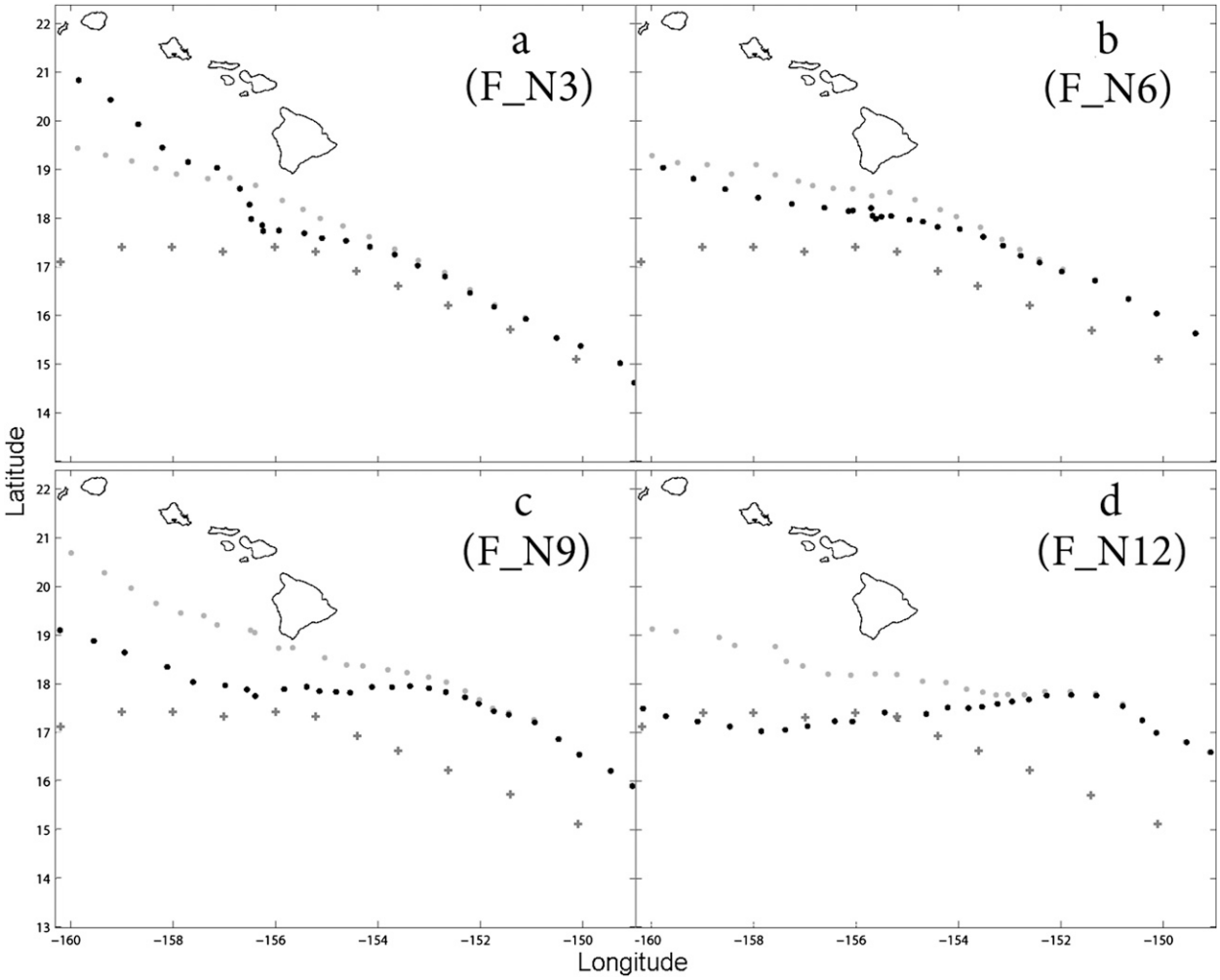

FIG. 7. As in Fig. 4, but for (a) F_N3, (b) F_N6, (c) F_N9, and (d) F_N12.

and Dot (DotBI, DotBI_N2, DotBI_N4). A lag of the BI cases apparent in the track plots (Figs. 4 and 7), is evidence of this slowing; however, it is more clearly revealed by calculating the speed of movement of the surface low pressure center as shown in Fig. 8 for DotBI_0, DotBI_N4, FBI_0, and FBI_N3. Generally the closer a TC approaches to the east of the BI the greater the slowing of motion. In all of the simulations in Fig. 8 the hourly translational speed is less than that of the corresponding case with the BI removed for the first 30 h.

Yeh and Elsberry (1993) found zonal decelerations for TCs approaching Taiwan explained by enhanced blocking of the environmental flow advecting the cyclone. Figure 9 shows the blocking of the lower-tropospheric flow for the Dot and Flossie cases before the TCs are close to the island. Stronger flow occurs around the northern and southern tips of the BI with a relatively calm wake spreading downstream (southwestward). Deceleration of the flow below 3 km, upstream of the island, can also be seen. This could contribute to some slowing of the forward progression of the storm if its circulation moves into this region. Since the island blocking is confined mainly to the lower troposphere, it follows that a TC whose steering is governed more by the flow in the lower troposphere, should be affected the most by island blocking. The Flossie simulated storms weaken as they pass south of the BI (Fig. 10), because of the large-scale environment shear. If the shear-induced weakening leads to a TC whose top is blown off to the northeast (in the southwesterly upper-level flow) then the track of the low-level center will be determined more by the lower-tropospheric flow. This appears to be what happened in reality (Fig. 3d), but is not as apparent in simulations FBI_0, FBI_N3, and FBI_N6. Therefore to better establish the reasons for the southward deviations in these simulations it is better to consider steering over a deeper layer.

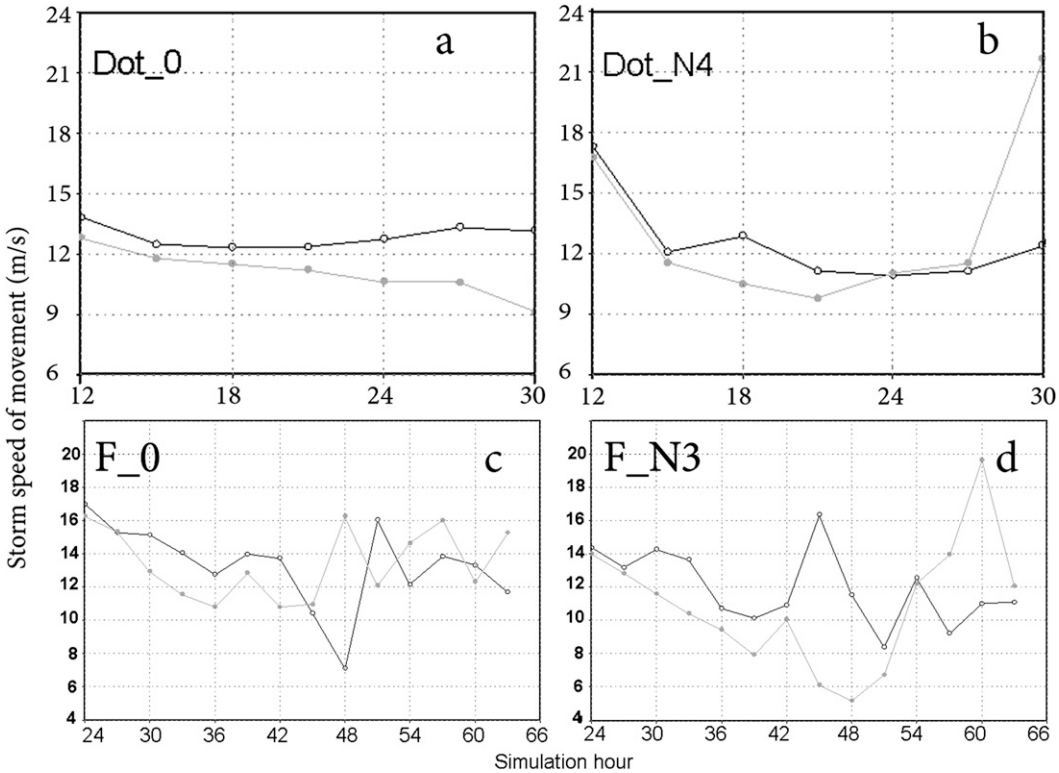

FIG. 8. Hourly translational speeds (m s^{-1}) of TC center for Dot simulations (a) Dot_0 and (b) Dot_N4 and Flossie simulations (c) F_0 and (d) F_N3. The light gray (black) lines are the cases with (without) the BI.

To investigate this further, the mass-weighted steering flow between 850 and 400 hPa for a hurricane, and between 850 and 700 hPa for a tropical storm, is calculated consistent with Gross (1991). This is done on equally spaced pressure (50-hPa spacing) levels for the zonal and meridional components using the following equations for hurricane steering:

$$\frac{(u_{850} + u_{800} + \cdots + u_{400})}{10}, \quad (1)$$

$$\frac{(v_{850} + v_{800} + \cdots + v_{400})}{10}. \quad (2)$$

The subscripts of the zonal u and meridional v winds designate the pressure level. The steering flow difference can then be calculated by subtracting the steering flow for the no-BI case from that of the BI case. Figure 11 shows the steering flow difference for hours 12–24 of the control Flossie simulations. The tropical storm steering flow difference shows a greater northerly component to the southeast of the BI than the hurricane steering flow. The implication is that if a hurricane weakens close to the south of the BI then it will be increasingly deviated to the south. This would happen anyway since the low-level trade wind steering flow is toward the southwest. Figure 11, however, suggests an additional southward steering caused by the island.

For FBI_N3 and FBI_N6 the sharp slowing south of the BI has consequences for the intensity of the storm once it passes west of the BI. Taking F_N6 as an example, Fig. 10b shows early weakening in FBI_N6 is small and by hour 42 both FBI_N6 and FnoBI_N6 maintain similar central pressures with the former ending up only slightly weaker by hour 66 onward. However, since FBI_N6 slows down to very slow translational speeds (less than 4 m s^{-1} between hours 45 and 52) as it passes south of the BI, there is more time for weakening to occur before it passes to the west. Consequently FBI_N6 is much weaker at longitudes west of the BI than FnoBI_N6. For example when the storms pass west of 157°W, FBI_N6 has a central pressure of 1008 hPa compared to 998 hPa for FnoBI_N6. Therefore, even though the weakening rates are similar with and without the island a slowing of track can lead to a weaker storm at longitudes west of the BI.

For the cases that track closest to the island (e.g., DotBI_N4, FBI_0, and FBI_N3 in Figs. 8b–d, respectively), the storms accelerate after passing the point nearest to the island (e.g., after hour 20 for DotBI_N4 in Fig. 8b). This

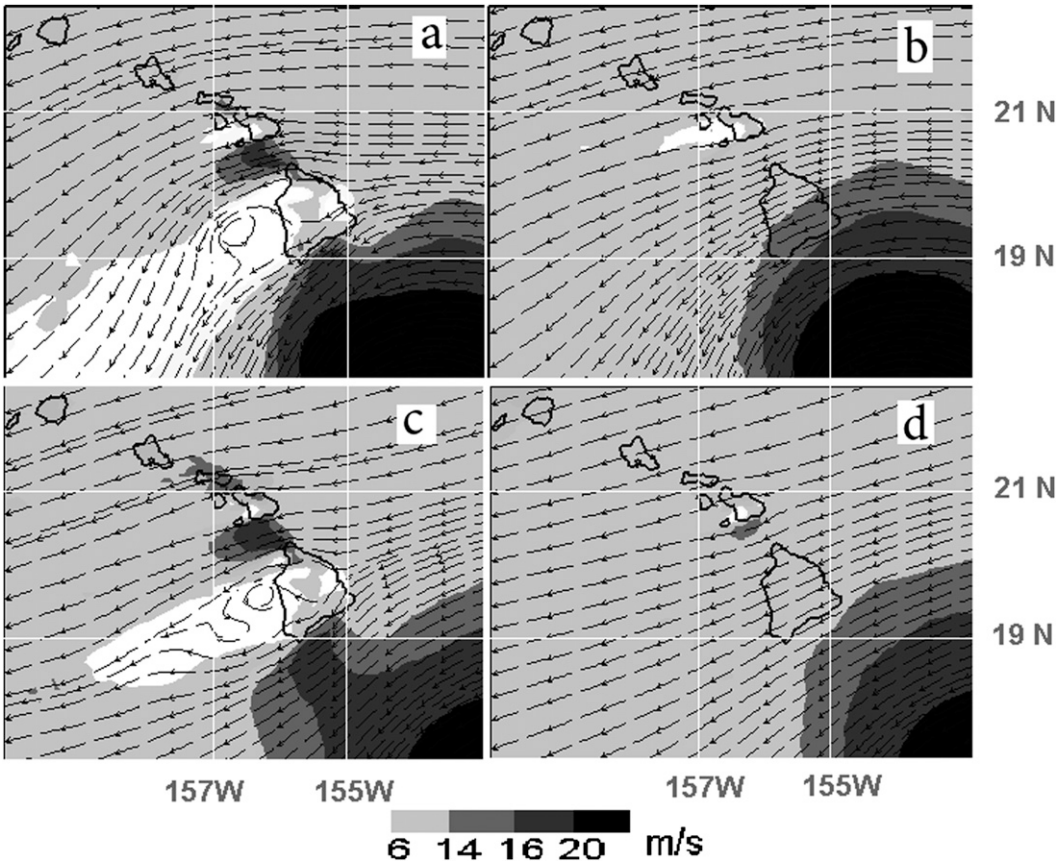

FIG. 9. Simulated wind (m s^{-1}) fields averaged from hours 12–24 and from levels 1–10 (0–3.4 km over open ocean) for (a) DotBI_0, (b) DotnoBI_0, (c) FBI_0, and (d) FnoBI_0.

leads to equal or greater translational speed, at least temporarily, than the cases with the BI removed, in the region to the southwest of the BI.

b. *Southward track deviation as a TC approaches the BI from the east*

A robust feature of simulated TCs that approach the BI from the east is a southward deviation of track. Southward deviations of TCs approaching Taiwan have been found in previous studies (e.g., Chang 1982; Yeh and Elsberry 1993; Lin et al. 1999, 2005). The magnitude and persistence of this southward deviation varies between the simulations. The largest deviations occur for simulations FBI_N9 and FBI_N12 (Figs. 7c,d) with both simulations ending up over 1.5° latitude farther south than FnoBI_N9 and FnoBI_N12, respectively.

FBI_0 deviates 45 km southward near 156°W. Figure 11 shows that this deviation occurs where the steering flow difference has its largest northerly component. Between 154° and 156°W the hurricane steering flow difference is northerly with a magnitude between 0.2 and 0.5 m s^{-1}. Since the TC is within this region for approximately 24 h, this would correspond to a southward displacement of between 17.3 and 43.2 km.

In the FBI_N3 case, the model TC begins to deviate to the south at 153°W (Fig. 7a). The maximum deviation occurs near 156°W where FBI_N3 lies 100 km to the south of FnoBI_N3. This larger southward deviation compared to FBI_0, is due to the closer approach to the BI as can be inferred from the larger environmental steering difference closer to the island as shown in Fig. 11. In addition, since the TC movement is slower, the storm will remain longer in this region and thus the deviation will be greater. The complicated direct interaction of the TC with the BI needs to be considered as well. In idealized studies Lin et al. (2005) found that a jet of northerly winds forming between a cyclone and an island mountain range induces northerly advection of vorticity that can deviate a cyclone southward. This might be acting to increase the southward deviation over that of just the blocking of the environmental flow. Conversely island-induced moist processes can act to deviate the TC northward (Wu 2001). Sensitivity studies could be performed to establish the relative importance of these effects.

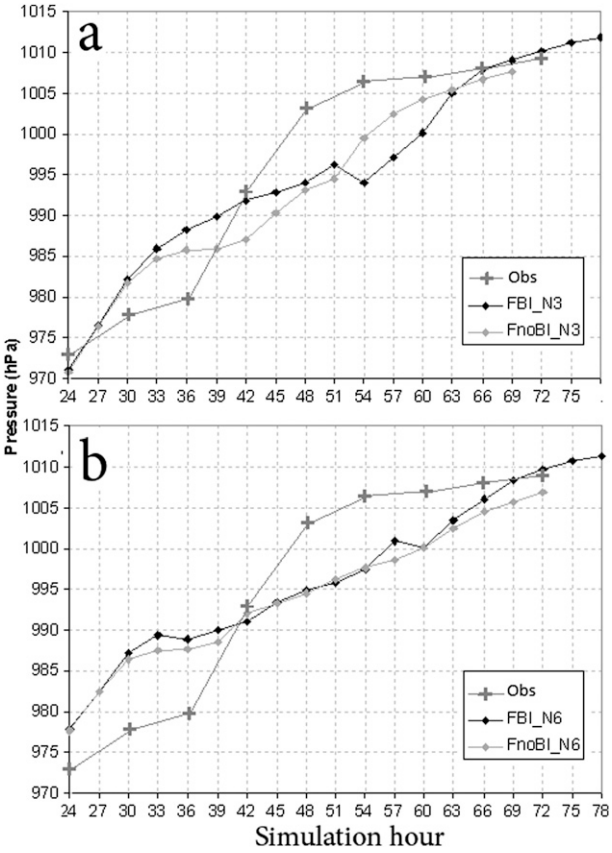

FIG. 10. Evolutions of minimum sea level pressures for Flossie simulations: (a) F_N3 and (b) F_N6. The lines end after the storm center exits domain 2.

c. *Contraction of core structure when approaching to south of the BI*

The simulations of TCs passing close to the southeast of the BI reveal a tendency toward a reduced radius of maximum winds (RMW) and a more axisymmetric wind speed field. These phenomena occur most starkly for simulations FBI_N3 and FBI_N6 and to a lesser degree in the Dot simulations. Greater weakening of FBI_N3, compared to FnoBI_N3, occurs from hours 30–42 (Fig. 10a). However when the storm makes its closest approach to the BI (hour 54), FBI_N3 has a 5-hPa lower central pressure than FnoBI_N3. Some factor has enabled FBI_N3 to maintain its intensity from hours 45–54 while FnoBI_N3 steadily weakens. After hour 54 rapid weakening of FBI_N3 occurs and the central pressure ends up slightly higher than FnoBI_N3 by hour 66.

In the case of FBI_N6 there are only small differences in central pressure with FnoBI_N6 (Fig. 10b); however, structural changes do occur. Figure 12 shows the progression of the FBI_N6 and FnoBI_N6 simulations as the storm passes south of the island. By hour 39 FBI_N6 has precipitation surrounding the core indicating the formation of a large eye, whereas FnoBI_N6 has precipitation confined mostly to its northeastern quadrant. This pattern in FnoBI_N6 is consistent with a hurricane in an environment of strong southwesterly vertical shear. Six hours later FBI_N6 has maintained its eyewall but a reduction in the radial extent of the precipitation is occurring. This represents a contraction of the core convection that continues through hour 60 as the storm stalls to the south of the island. By comparison FnoBI_N6 maintains asymmetries in precipitation. Similar structural changes occur in simulations FBI_N3 and FnoBI_N3 (not shown).

What causes the contraction and axi-symmetrization of these storms? Figure 13 compares the surface wind field for FBI_N3 and FBI_N6 with their no-BI counterparts at similar longitudes when the storms lie close to the BI. Blocking of airflow by the island orography can be seen to be reducing the storm wind speed to the north of the storm core in both FBI_N3 and FBI_N6. As a result, a more symmetric and compact wind field develops in the storm core. Bender et al. (1985) found that upstream of an idealized mountain range convergence of moisture acted to maintain intensity. In our simulations Fig. 14 shows that greater moisture convergence persists for a longer period (up to hour 60) with the BI present. This extended period of enhanced low-level moisture convergence is possibly attributed to stronger cyclonic vorticity forcing (due to the core contraction) at top of the planetary boundary layer.

d. *Rightward deviation of track after passing south of the BI*

After deviating southward on approach to the BI, many of the simulated storms then exhibit a deviation to the right after passing to the west of the BI. Cases that produce this phenomenon are DotBI_0, DotBI_N2, DotBI_N4, FBI_0, FBI_N3, IBI_N3, and IBI_0.

The Flossie cases FBI_0 and FBI_N3 produce northward deviations to the west of the BI that do not agree with the observed track. Figure 3 and the forecast discussions show that the real storm was sheared apart leaving an exposed low-level circulation that advected southwestward in the low-level flow since the optimum steering layers for weaker storms are in the lower troposphere (Velden 1993). In contrast, the model TC maintains core convection for longer and consequently retains better vertical coherence. As shown in Fig. 5 the simulated storm has a larger area of strong winds than the observed storm. The total angular momentum of the storm is therefore higher at this time and so it may take longer to spin down and weaken under the given unfavorable conditions. The consequence is that the storm core penetrates into the lee of the island where the low level northeasterly steering

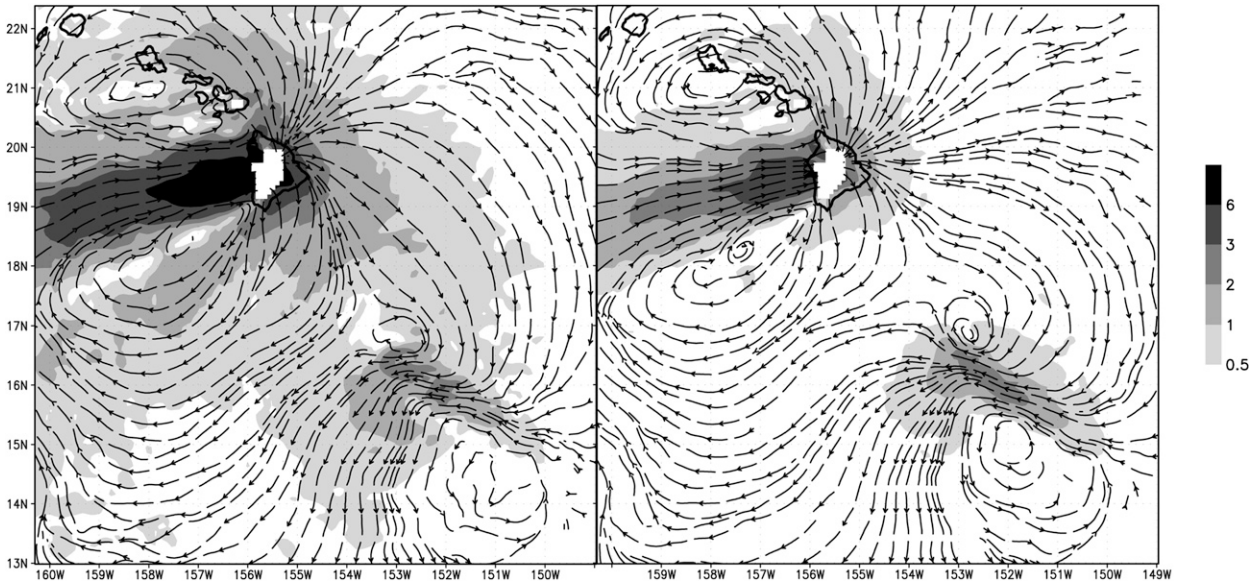

FIG. 11. The difference between the BI and no BI experiments (FBI_0 vs FnoBI_0) of the vertically averaged steering flow (shading denotes the wind speed difference, m s^{-1}) for (left) a shallower ''tropical storm'' layer (850–700 hPa) and (right) a deeper ''hurricane'' layer (850–400 hPa) averaged from hours 12–24.

flow suddenly becomes much less strong (Fig. 9c) leading to a northward track deviation.

The northward deviation west of the BI of DotBI_0 (Fig. 4a) agrees better with observations than DotnoBI_0 although both fail to reproduce Kauai landfall. This suggests that the BI is responsible for part of the northward deviation observed in reality. The Iniki cases indicate a more remote BI forcing on hurricane track. The southwestward deviations in the BI cases are followed by a sharper turning to the right beginning near 158°W (Figs. 4e,f). For IBI_0 this additional turning is only enough to bring the storm center roughly back to the position of InoBI_0 by the time the storms pass through the Kauai Channel, although IBI_0 does lag InoBI_0 by 6 h. For IBI_N3 the turning is sharper so that near 20°N it has passed to the east of InoBI_N3. By the time IBI_N3 is north of Oahu it is located some 115 km to the east of InoBI_N3.

It is hypothesized that these differences in track are predominantly due to differences in the lower-tropospheric flow induced by the BI. In particular the transition from stronger northeasterly flow, which spreads southwestward from the south side of the BI, to weaker flow in the wake region, fits with the location of the transition from a left-deviated to a right-deviated track. In addition as the storms pass 19.5°N, IBI_0 and IBI_N3 undergo a subtle shift to the left, which does not occur in the cases with no BI. This occurs as the storms encounter stronger low-level northeasterly flow that has funneled through the Alenuihaha Channel between the BI and Maui.

To investigate these track changes further, the deep-tropospheric steering flow difference is plotted for the earlier hours of the Iniki simulations in Fig. 15. The deviation in track to the left occurs where the steering flow difference is weakly northerly due to stronger northeasterly flow south of the BI. The sharper deviation to the right seen between 18° and 20°N in Fig. 4f occurs as the TC enters the region of westerly steering flow difference. IBI_N3 deviates right more than IBI_0 because of stronger westerly steering flow difference closer to the BI. The situation is complicated by how the flow near the island changes as the storm impacts the regional winds. This leads to a northward shift in the wake position as the lower-tropospheric winds over the BI turn more southeasterly. This might explain the continued eastward deviation seen for IBI_N3 north of 20°N.

e. Greater intensity in lee (west) of the BI

In addition to the rightward-track deviations west of the BI, simulations IBI_0 and IBI_N3 also exhibit intensity changes. Figure 16 shows that after hour 54 the IBI_0 and IBI_N3 pressure traces begin to significantly diverge from those for InoBI_0 and InoBI_N3, respectively. This coincides with the time the tracks begin to deviate rightward as the storm begins to interact with the wake region to the west southwest of the BI. In the earlier hours of the simulation, the low-level northeasterly flow in this wake area is weaker (similar to Flossie and Dot in Fig. 9). Consequently the vertical wind shear is reduced (since the upper-level winds are southwesterly), as can be seen by

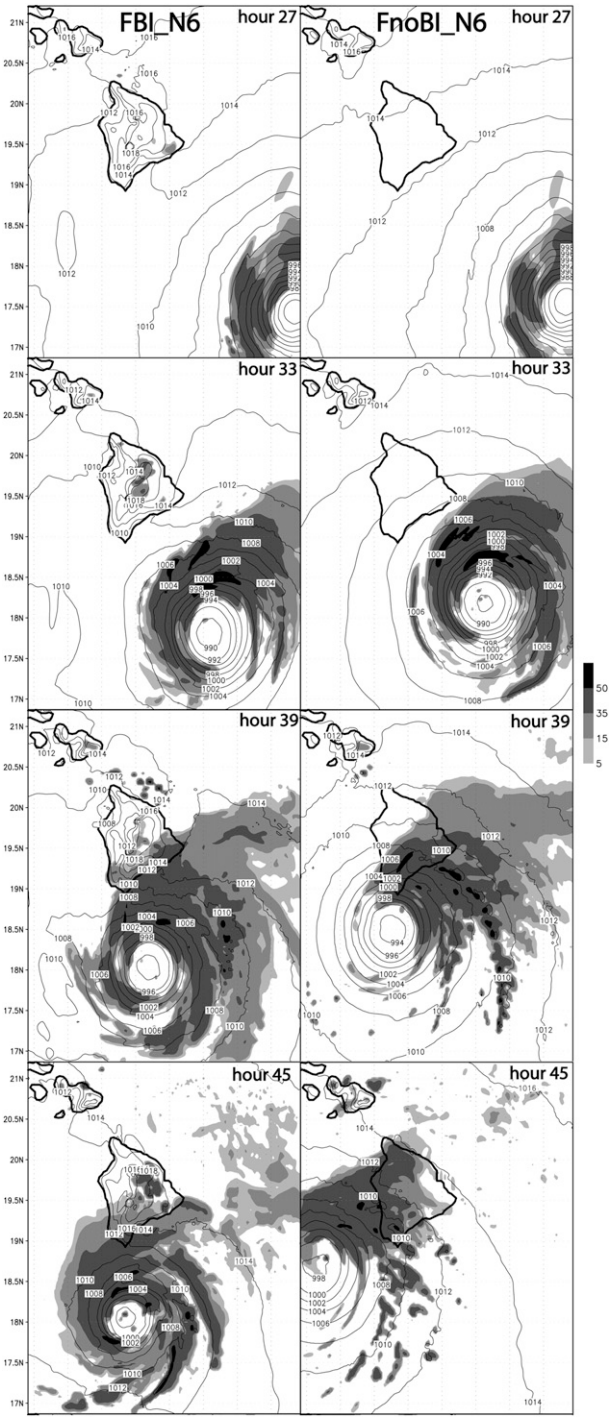

FIG. 12. Structure and evolution of simulated sea level pressure (contour interval: 2 mb) and radar reflectivity (shading, units: dBZ) at domain 3 for (left) FBI_N6 and (right) FnoBI_N6. The plots are 6-hourly, starting at hour 27.

comparing IBI_0 (Fig. 17a) with InoBI_0 (Fig. 17b). To determine the extent of BI influence on vertical shear, the difference in shear between IBI_N3 and InoBI_N3 is plotted in Fig. 17c. An easterly component of the wind shear difference indicates reduced wind shear because the large-scale vertical wind shear is westerly. Since the area of reduced shear spreads eastward from the BI, it covers an area south of the smaller islands.

Other factors may be involved; for example, the downstream propagation of vorticity features generated on the lee of the mountain could influence the structure of the TC circulation. Smith and Smith (1995) found that the interaction of a vortex with idealized topography in a shallow-water model leads to trailing regions of positive vorticity that can wrap into the primary vortex. Lin et al. (1999) showed in a primitive equation simulation of a drifting cyclone over an idealized topography, a pair of positive and negative vorticity centers generated on the lee side and shed downstream in a low Froude number example. Downstream vorticity features such as a prominent vorticity banner spreading southwestward from the northern edge of the island, are present in our simulations. Although not investigated in detail here, these features could have affected the intensity of the Iniki cases as they wrapped into the TC circulation during passage through the BI wake.

The intensity differences between IBI_N3 and InoBI_N3 are significant. For example at hour 66 IBI_N3 central minimum pressure is more than 10 hPa lower than that of InoBI_N3. The IBI_N3 case makes landfall on Oahu at hour 76 by which time it has undergone an accelerated weakening, but is still 6 hPa more intense than InoBI_N3. This suggests that although other cases show a potential protective effect of the BI for the rest of Hawaiian islands, in this case the effect is to increase the hazard. These simulated storms move closer to the BI than Hurricane Iniki actually did; however, when the effects of all the island wakes are considered, and given the magnitude of the intensity differences seen here, it appears possible that Iniki would have been weaker when it reached the latitude of Kauai, had the Hawaiian Islands not existed. Given the potential impact of storms similar to IBI_0 and IBI_N3 on the Hawaiian Islands, these speculations warrant future observational and modeling research.

5. Conclusions

The central Pacific near the Hawaiian Islands is often an unfavorable environment for tropical cyclones and therefore they frequently weaken and dissipate in this region. This is due to 1) the frequent presence of strong vertical wind shear associated with an upper-level trough and lower-level trade winds, 2) marginal sea surface temperature, and 3) a dry midlevel environment. In addition to these factors this research has shown that the role of the substantial topography of the Hawaiian Islands needs

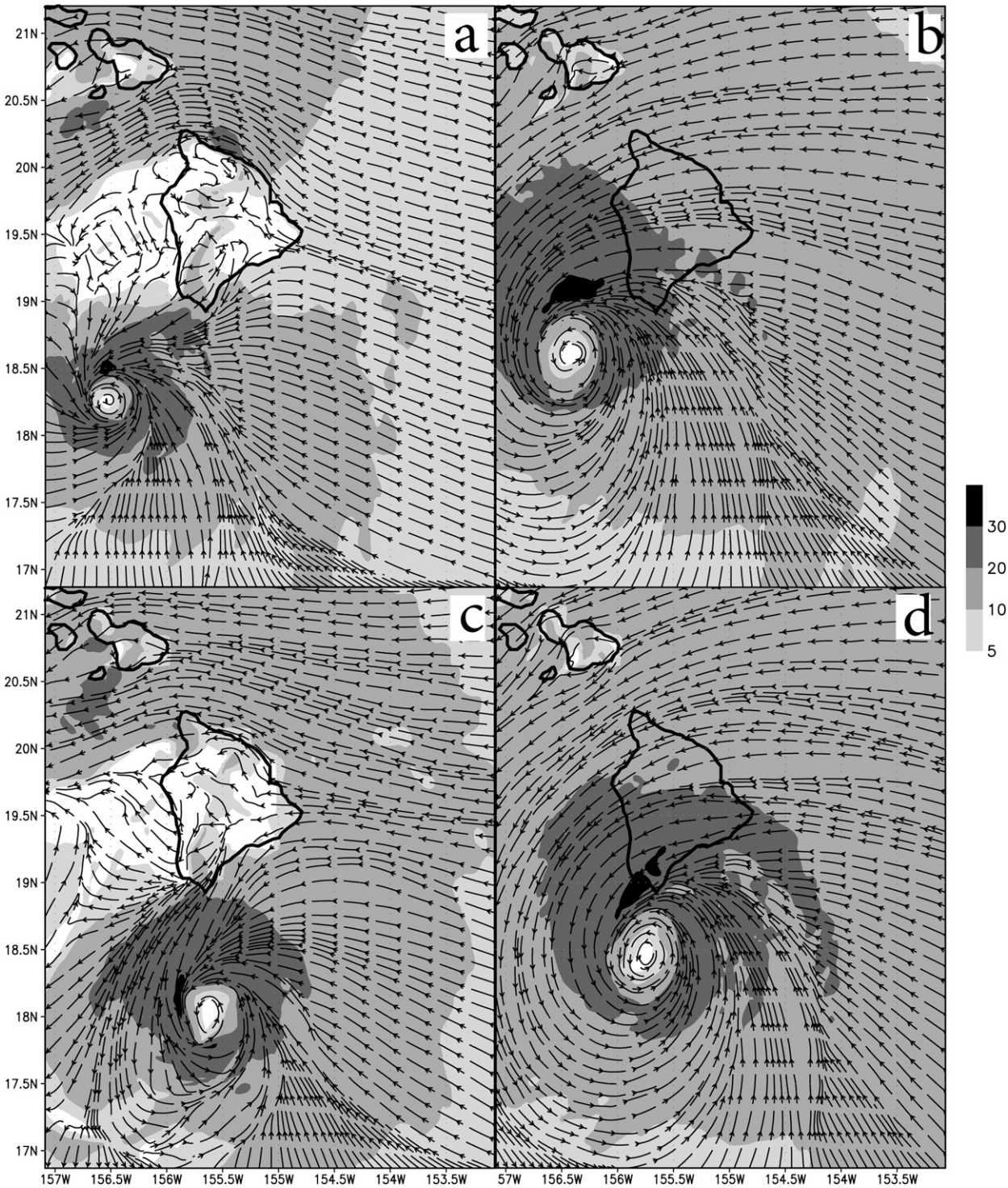

FIG. 13. Simulated 10-m wind speeds (shading, m s^{-1}) and streamlines (vector) for (a) FBI_N3 at hour 57, (b) FnoBI_N3 at hour 48, (c) FBI_N6 at hour 54, and (d) FnoBI_N6 at hour 45.

to be considered when forecasting or investigating storms that pass close to the state.

The simulations of tropical cyclones that pass near or over the Big Island reveal this island's potential influence on storm characteristics. The results suggest that a number of topographically forced phenomena occur because the Big Island is strongly rooted in a flow-splitting regime as a tropical cyclone approaches. A slowing of track is

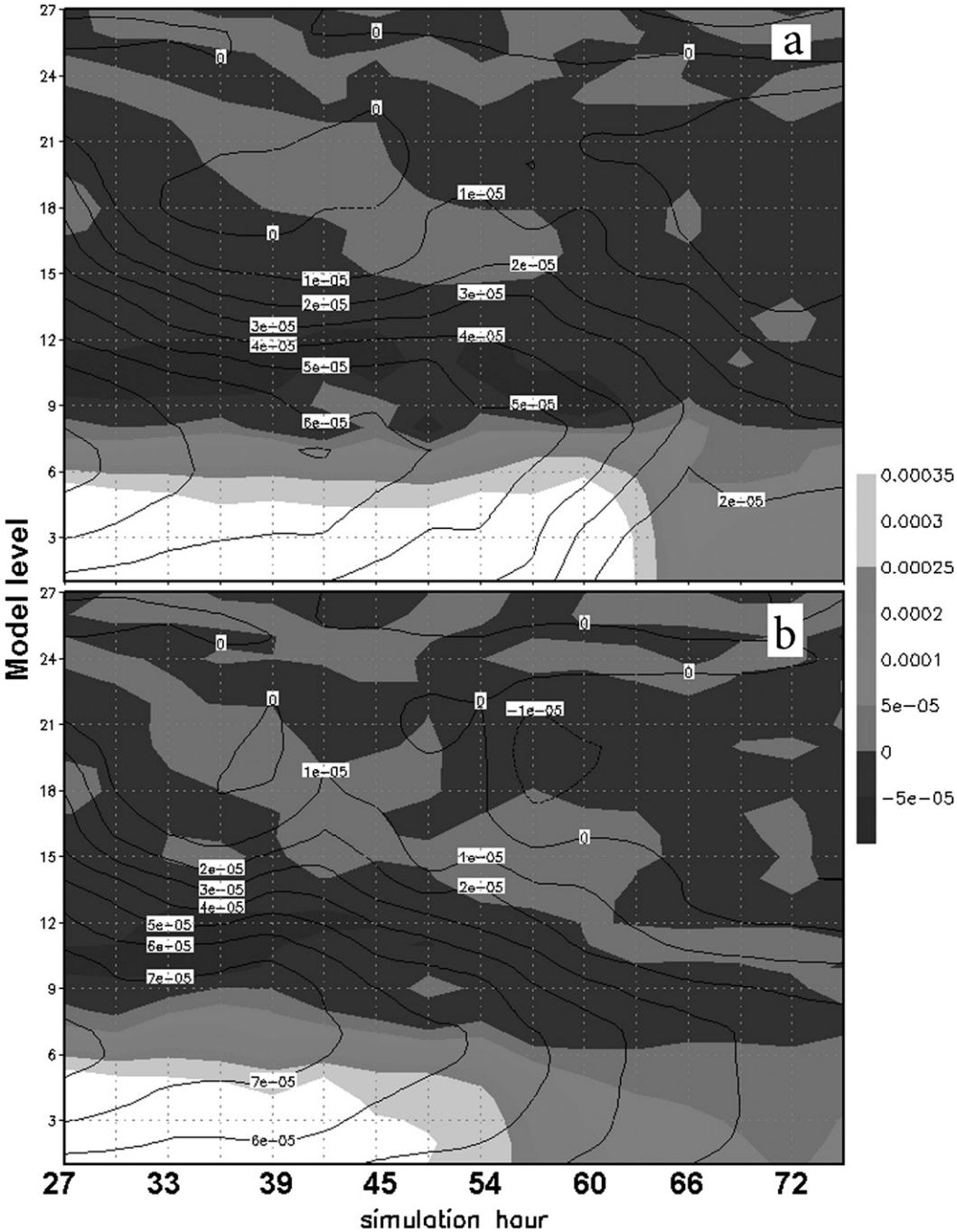

FIG. 14. Time–vertical section of area-averaged (153 km by 153 km) moisture convergence (s^{-1}, shades) and vorticity (s^{-1}, contours) centered on the minimum surface pressure for (a) FBI_N3 and (b) FnoBI_N3. Positive values denote the moisture convergence.

robustly observed for storms approaching from the east. This is associated with a westerly steering anomaly caused by island blocking. Tracks to the south of the island are observed to first deviate south because of the region of enhanced northeasterly flow that forms off the south of the Big Island due to island blocking. In addition, for storms passing very close to the island, the interaction of the storm circulation with the island leads to a number of structural and track changes. In particular the axi-symmetrization in two of the Hurricane Flossie

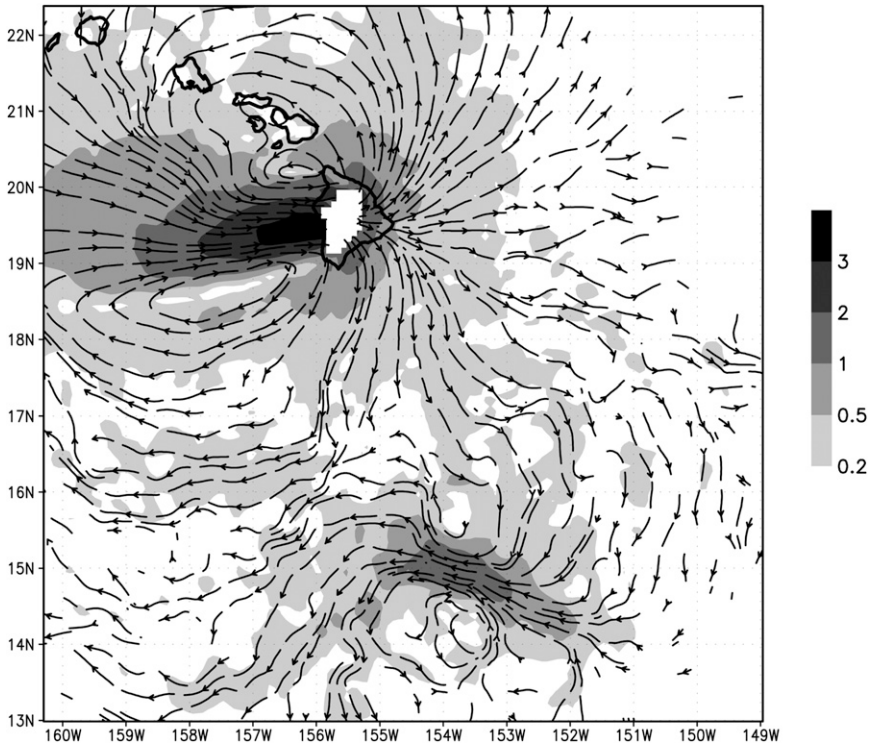

FIG. 15. The vertically averaged (850–400 hPa) steering flow difference between IBI_N3 and InoBI_N3 (m s^{-1}) averaged from hours 12–24.

simulations, caused primarily by the blocking of the stronger easterly flow in the north of the storm, is proposed as being the mechanism that led the real storm to develop an eye unexpectedly as it approached from the southeast.

Some storms that pass south of the Big Island then deviate to the north as they move into a strong westerly steering anomaly associated with weak winds in the island wake. The wake of the island can also cause track and intensity changes that are observable far from the island. It is proposed that stronger intensities occur in the wake associated with weakened vertical wind shear. Therefore, although the Big Island appears to play a predominantly protective role for the other islands for storms approaching from the east, it may act to increase the hazard for storms moving up from the south. In the case of Hurricane Dot, we propose that the Big Island contributed to the more northerly track that led to its eventual landfall on Kauai.

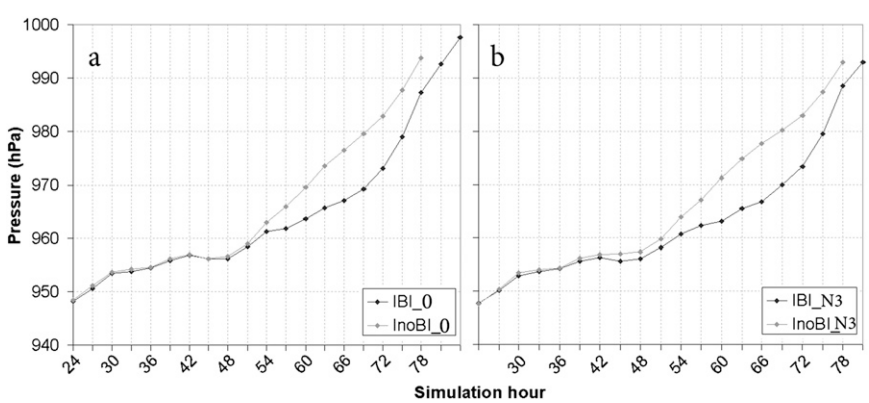

FIG. 16. Evolution of simulated minimum sea level pressure (hPa) for (a) I_0 and (b) I_N3 cases. In the BI cases, the storm centers remain on domain 2 for a slightly longer period.

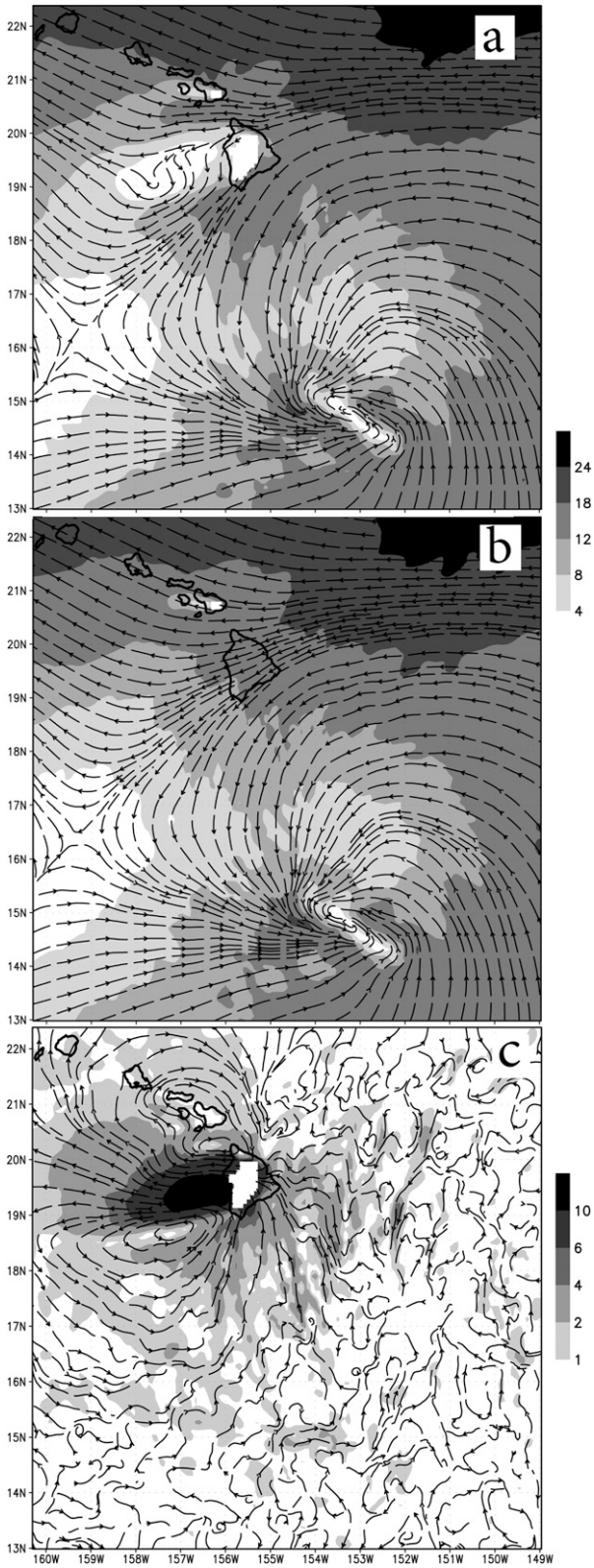

FIG. 17. Simulated vertical wind shear (m s^{-1}) between 850 and 200 hPa averaged from hours 12–24 for (a) IBI_N3 and (b) InoBI_N3 cases. (c) The difference of the vertical wind shear between IBI_N3 and InoBI_N3.

Acknowledgments. Discussions with Bob Ge, Michael Murphy, Gary Barnes, and Steven Businger are greatly appreciated. This work was supported by ONR Grants N000141010774, N000140810256, N000140510551, and N000140810450, NRL Grant N00173091G008, and by the International Pacific Research Center that is partially sponsored by the Japan Agency for Marine-Earth Science and Technology (JAMSTEC), NASA (NNX07AG53G), and NOAA (NA17RJ1230).

REFERENCES

Bender, M., R. E. Tuleya, and Y. Kurihara, 1985: A numerical study of the effect of a mountain range on a landfalling tropical cyclone. *Mon. Wea. Rev.,* **113,** 567–583.

Betts, A. K., and M. J. Miller, 1986: A new convective adjustment scheme. Part II: Single column tests using GATE wave, BOMEX, and arctic air-mass data sets. *Quart. J. Roy. Meteor. Soc.,* **112,** 693–709.

Chambers, C. R. S., 2008: Effect of mesoscale orography on tropical cyclones near Hawai'i's Big Island and in the South China Sea. Ph.D. dissertation, University of Hawaii at Manoa, 165 pp.

Chang, S. W., 1982: The orographic effects induced by an island mountain range on propagating tropical cyclones. *Mon. Wea. Rev.,* **110,** 1255–1270.

Chen, Y.-L., and J. Feng, 2001: Numerical simulations of airflow and cloud distributions over the windward side of the island of Hawaii. Part I: The effects of trade wind inversion. *Mon. Wea. Rev.,* **129,** 1117–1134.

Dvorak, V. F., 1984: Tropical cyclone intensity analysis using satellite data. NOAA Tech. Rep. NESDIS 11, U. S. Dept. of Commerce, Washington, DC, 47 pp.

Gray, W. M., 1975: Tropical cyclone genesis. Department of Atmospheric Sciences Paper 232, Colorado State University, Fort Collins, CO, 121 pp.

Gross, J. M., 1991: The effect of shallow, medium, and deep layer mean wind in the beta and advection model. Preprints, *19th Conf. on Hurricanes and Tropical Meteorology,* Miami, FL, Amer. Meteor. Soc., 104–106.

Hill, K. A., and G. M. Lackmann, 2009: Influence of environmental humidity on tropical cyclone size. *Mon. Wea. Rev.,* **137,** 3294–3315.

Jian, G.-J., and C.-C. Wu, 2008: A numerical study of the track deflection of Supertyphoon Haitang (2005) prior to its landfall in Taiwan. *Mon. Wea. Rev.,* **136,** 598–615.

Knaff, J. A., C. R. Sampson, M. DeMaria, T. P. Marchok, J. M. Gross, and C. J. McAdie, 2007: Statistical tropical cyclone wind radii prediction using climatology and persistence. *Wea. Forecasting,* **22,** 781–791.

Lin, Y.-L., R. D. Farley, and H. D. Orville, 1983: Bulk parameterization of the snow field in a cloud model. *J. Climate Appl. Meteor.,* **22,** 1065–1092.

——, J. Han, D. W. Hamilton, and C.-Y. Huang, 1999: Orographic influence on a drifting cyclone. *J. Atmos. Sci.,* **56,** 534–562.

——, S.-Y. Chen, C. M. Hill, and C. Y. Huang, 2005: Control parameters for the influence of a mesoscale mountain range on cyclone track continuity and deflection. *J. Atmos. Sci.,* **62,** 1849–1866.

Noh, Y., W. G. Cheon, S. Y. Hong, and S. Raasch, 2003: Improvement of the K-profile model for the planetary boundary layer based on large eddy simulation data. *Bound.-Layer Meteor.,* **107,** 421–427.

Roux, F., F. Chane-Ming, A. Lassere-Bigorry, and O. Nuissier, 2004: Structure and evolution of intense tropical cyclone Dina near La Reunion on 22 January 2002: GB-EVTD analysis of single Doppler radar observations. *J. Atmos. Oceanic Technol.,* **21,** 1501–1518.

Skamarock, W. C., J. B. Klemp, J. Dudhia, D. O. Gill, D. M. Barker, W. Wang, and J. G. Powers, 2005: A description of the Advanced Research WRF version 2. NCAR Tech. Note 468-STR, 88 pp.

Smith, R. B., 1989: Hydrostatic airflow over mountains. *Advances in Geophysics,* Vol. 31, Academic Press, 1–41.

——, and D. F. Smith, 1995: Pseudoinviscid wake formation by mountains in shallow-water flow with a drifting vortex. *J. Atmos. Sci.,* **52,** 436–454.

Smorlarkiewicz, P. K., and R. Rotunno, 1989: Low Froude number flow past three-dimensional obstacles. Part I: Baroclinically generated lee vortices. *J. Atmos. Sci.,* **46,** 1154–1164.

Velden, C. S., 1993: The relationship between tropical cyclone motion, intensity, and the vertical extent of the environmental steering layer in the Atlantic Ocean. Preprints, *20th Conf. on Hurricanes and Tropical Meteorology,* San Antonio, TX, Amer. Meteor. Soc., 31–34.

Wang, Y., 1995: An inverse balance equation in sigma coordinates for model initialization. *Mon. Wea. Rev.,* **123,** 482–488.

Wu, C.-C., 2001: Numerical simulation of Typhoon Gladys (1994) and its interaction with Taiwan terrain using the GFDL hurricane model. *Mon. Wea. Rev.,* **129,** 1533–1549.

Xu, J., and Y. Wang, 2010: Sensitivity of the simulated tropical cyclone inner-core size to the initial vortex size. *Mon. Wea. Rev.,* **138,** 4135–4157.

Yeh, T.-C., and R. L. Elsberry, 1993: Interactions of typhoons with the Taiwan orography. Part I: Upstream track deflection. *Mon. Wea. Rev.,* **121,** 3193–3212.